J. Fluid Mech. (1996), *vol.* 309, *pp.* 157–182

An experimental and theoretical study of the turbulent coflowing jet

By T. B. NICKELS AND A. E. PERRY

Department of Mechanical and Manufacturing Engineering,
University of Melbourne, Parkville, Vic. 3052, Australia

(Received 29 September 1994 and in revised form 15 September 1995)

Experiments carried out recently on a family of axisymmetric coflowing turbulent jets with different nozzle to free-stream velocity ratios are described. Special care was taken to ensure top-hat velocity profiles at the nozzle exit so as to reduce the number of parameters associated with the initial conditions. This results in a collapse of the data without the need to introduce different effective origins for the streamwise coordinate. The mean flow behaviour is compared to self-preserving asymptotic forms and stresses are also examined to investigate the possibility of self-preservation. Comparisons are made with measurements of other workers in coflowing jets and axisymmetric wakes. Further information on the structure of the coflowing jet is found by examining the spectral Reynolds shear stress correlation coefficient, the premultiplied spectra and the high-wavenumber forms of the spectra. An analysis was carried out to see if the mean flow, Reynolds stress distributions and spectra are consistent with an inviscid 'double-roller' vortex structure for the representative large-scale energy-containing motions. Results show support for such a model.

1. Introduction

This paper presents some experimental results and observations from a study of an axisymmetric turbulent jet issuing into a parallel moving airstream. The particular flow of interest consists of a turbulent jet issuing into a slow-moving, constant-velocity (U_1), outer flow of infinite extent (as opposed to the flow of a jet in a finite duct, or the flow of coaxial jets). Here this flow case will be referred to as a 'coflowing jet'.

This flow case is of interest for several reasons. One is that it is postulated that in this flow, at a sufficient distance from the nozzle, the jet should 'forget' its initial conditions and therefore only be determined by the net momentum excess (or the momentum radius, θ, which is invariant with streamwise distance in the absence of external pressure gradients) and local conditions (e.g. the local jet radius, Δ, and local velocity excess, $U_o = U_{CL} - U_1$, where U_{CL} is the velocity on the jet centreline and U_1 is the velocity of the external stream). If this is true, then measurements from different coflowing jets should collapse when scaled with these parameters. It further suggests the possibility of a self-preserving flow at large distances from the nozzle. This possibility is supported by analysis which suggests that the flow may be asymptotically self-preserving in the limit of vanishingly small local velocity excess.

The coflowing jet also provides a useful flow case for studying the structure of jets in general since the coflow removes the possibility of the backflow experienced in a free jet and also avoids the problems of measuring the almost zero velocities which occur in free jets at the edge of the shear layer. In this paper the possibility of

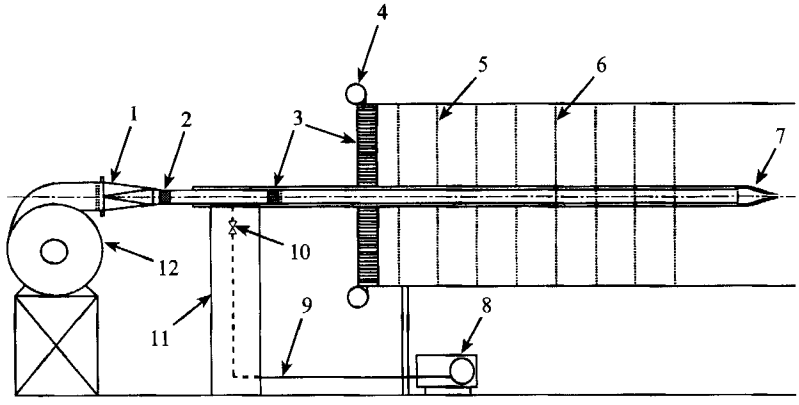

FIGURE 1. Layout of jet apparatus: 1. transition piece, 2. rubber membrane coupling, 3. honeycomb, 4. bell-mouth, 5. screen with hole, 6. screen passing through jet, 7. nozzle, 8. vacuum pump, 9. suction line, 10. needle valve, 11. aerofoil support, 12. centrifugal fan.

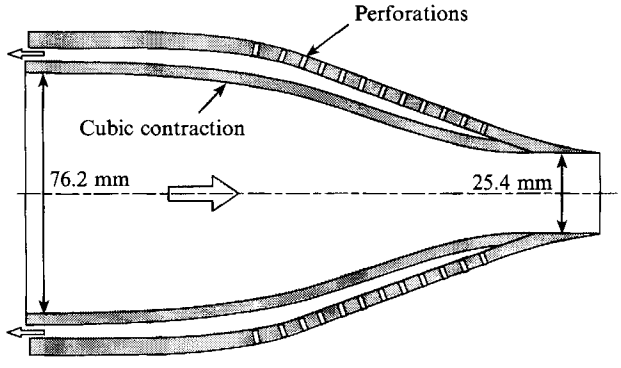

FIGURE 2. Details of the jet nozzle used.

self-preservation for this flow case is discussed and some comments on the structure of jets are made based on spectral measurements which are shown. A 'double-roller' vortex model similar to that proposed by Townsend is investigated and found to be consistent with experimental data.

2. Apparatus and experimental techniques

The apparatus used in this study is shown in figure 1. The wind-tunnel cross-section is 1.22 m wide by 0.89 m high with a maximum velocity of 3.5 m s^{-1} and a turbulence intensity of less than 0.6%. The jet issues from a 25.4 mm nozzle aligned with the wind-tunnel centreline. The nozzle has a contraction ratio of 9:1 which gives a turbulence intensity of less than 0.5% at the outlet. The exterior of the nozzle has perforations which allow for boundary layer suction to avoid separation of the flow on the outer surface as shown in figure 2. Flow in the jet is produced by a centrifugal blower through honeycomb and a series of screens. The blower is attached to the apparatus by a thin flexible coupling which isolates the nozzle from vibrations. The jet flow could be varied in the range 0–35 m s^{-1}.

Mean flow measurements were made using both Pitot-static tubes and dynamically calibrated hot wires. Static pressure measurements along the jet axis were made with the jet operating for all cases and showed the axial pressure gradient to be within

$\pm 1\%$. The hot-wire filaments were nominally 5 μm in diameter and 1mm long. Reynolds stresses were measured with dynamically calibrated 90° crossed wires and spectra were measured with uncalibrated crossed wires. The spectra were normalized so that

$$\int_0^\infty \psi_{ij}[f]\mathrm{d}f = \overline{u_i u_j} \tag{2.1}$$

where $\overline{u_i u_j}$ is the appropriate component of the Reynolds stress tensor. All of the spectra are displayed in terms of k_1 (the streamwise wavenumber) which is obtained using Taylor's hypothesis of frozen turbulence, i.e. $k_1 = 2\pi f/U_c$ where f is the frequency and U_c is some convection velocity here assumed to be equal to the local mean velocity of the flow at the point of interest. Such a spectral function is

$$p_{ij}[k_1] = \frac{U_c}{2\pi}\psi_{ij}[f]. \tag{2.2}$$

A final note is that $\phi_{ij}[k_1 l]$ represents the power spectral density per unit non-dimensional wavenumber $k_1 l$ which implies

$$\phi_{ij}[k_1 l] = \frac{p_{ij}[k_1]}{l} \tag{2.3}$$

where l is some length scale of interest and p_{ij} are the spectra for dimensional wavenumber k_1. In this paper ϕ_{11}, ϕ_{22} and ϕ_{33} will be referred to as the *normal* spectra and ϕ_{13} as the *co-spectra.*

Measurements of mean velocity, Reynolds stresses and spectra were taken at six streamwise positions for each flow case and at 17 cross-stream positions over the jet radius.

3. Experimental results

3.1. *Mean flow measurements*

Initial conditions

Mean velocity profiles taken at the nozzle ($x/D = 0.04$) are shown in figure 3. Here U_{oJ} is the velocity excess at the nozzle exit. It may be seen that the shape of the profiles for the two higher-λ_J cases is almost identical (where λ_J is the non-dimensional velocity excess at the nozzle exit, U_{oJ}/U_1) and the other case is not very different. In all cases, inner and outer boundary layers were laminar.

Decay of centreline mean velocity excess

If it is assumed that, at some distance from the nozzle, the flow becomes independent of the nozzle initial conditions and depends only on the momentum excess at the nozzle (as was suggested by Bradbury & Riley 1967), then it may be shown from dimensional considerations alone that

$$\lambda = F[x/\theta] \tag{3.1}$$

where λ is the local non-dimensional velocity excess ($\lambda = U_o/U_1$), x is the streamwise coordinate measured from the nozzle exit, F is a universal function and θ is the momentum radius of the jet as given by

$$\rho U_1^2 \theta^2 = \rho \int_0^\infty U(U - U_1)2\pi r \mathrm{d}r \tag{3.2}$$

where r is the radial coordinate measured from the jet axis. Figure 4 shows the

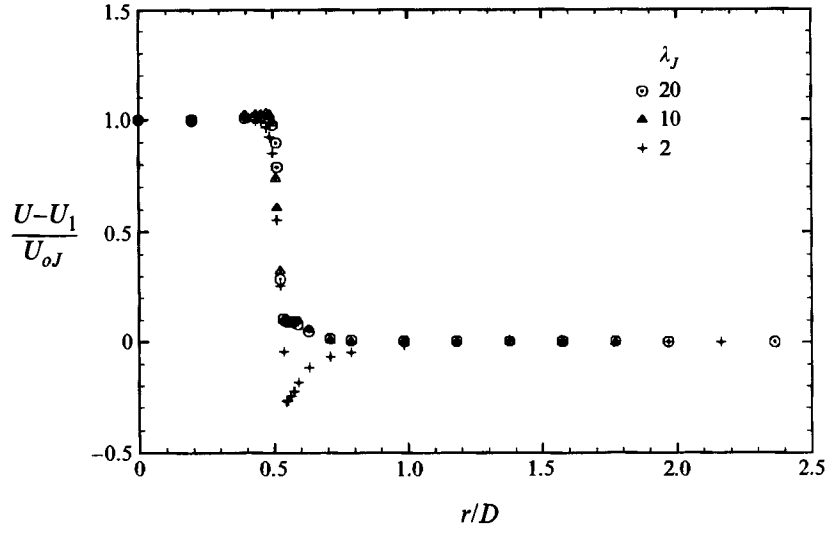

FIGURE 3. Mean velocity profiles at $x/D = 0.04$.

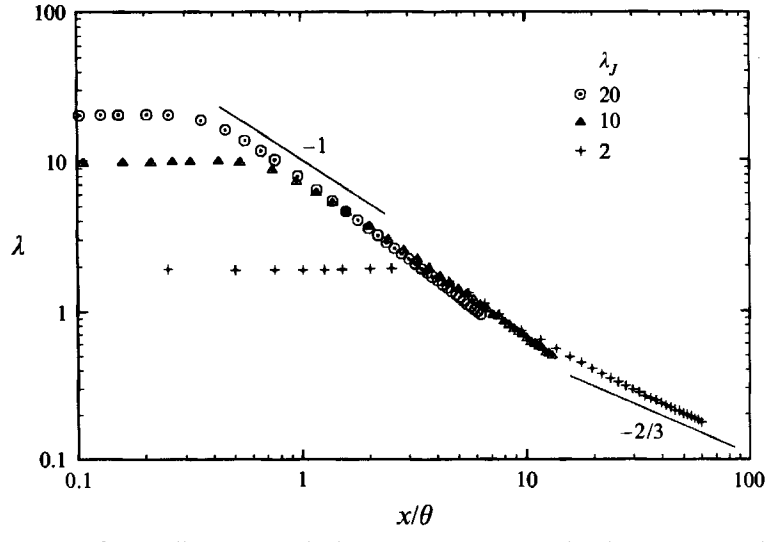

FIGURE 4. Decay of centreline mean velocity excess on a log scale, showing power-law asymptotes for self-preserving flows.

velocity decay for all three cases for x/θ values up to 60. It may be seen that (3.1) is satisfied reasonably well by the present data beyond the potential core. It is interesting to note that it was not necessary to correct these results for a shift in origin as has been done by other authors (eg. Bradbury & Riley 1967 and Challen 1968) which, it has been suggested, allows for the effect of different initial conditions. The most probable explanation for this is that in all three cases the initial profiles are similar in shape and close to the ideal *top-hat* profile. The only variable needed to specify the different initial conditions is λ_J and apparently this is quickly 'forgotten' as the flow evolves downstream. In fact the different cases collapse onto a single curve quite close to the end of the potential core. This result may be fortuitous but three quite different sets of data collapse reasonably well and support (3.1).

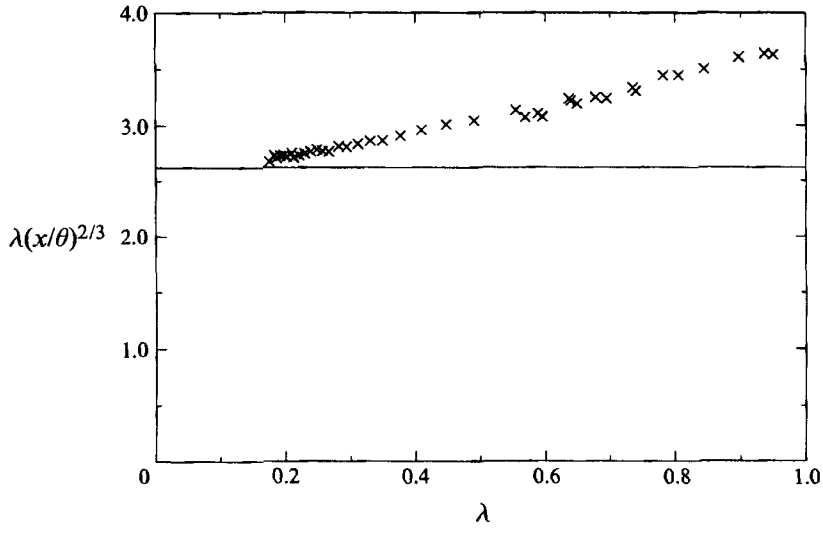

FIGURE 5. Centreline velocity excess premultiplied by $(x/\theta)^{2/3}$ versus λ.

Maczynski (1962), Tani & Kobashi (1951), Henbest & Yacoub (1991) and others have found the decay of the centreline velocity excess to be inversely proportional to the distance from the nozzle. The present results show that this is approximately valid only in the region close to the end of the potential core.

The log-log form of presentation in figure 4 is ideal for examining possible power-law forms for the decay. It may be seen that toward the nozzle (small x/θ) the decay appears to follow an x^{-1} law as would be expected if it approached the self-preserving form for a jet exhausting into still air. It may also be noted that at large x/θ it appears that the decay asymptotes to an $x^{-2/3}$ power law which is consistent with the behaviour of a self-preserving, small-excess jet. This does not imply that the flow is self-preserving in either case, but it demonstrates that the mean-flow behaviour is at least consistent with this possibility.

In order to further illustrate the behaviour at large x/θ, figure 5 shows the centreline velocity excess decay for the $\lambda_J = 2$ case premultiplied by $(x/\theta)^{2/3}$ and plotted *vs.* λ. It may be seen that the functional form does appear to asymptote to an $(x/\theta)^{-2/3}$ powerlaw as $\lambda \to 0$. Curve-fitting this data also allows an estimation of the constant in the $-2/3$ decay law (i.e. $\lambda = C(x/\theta)^{-2/3}$). The estimate shown was found using an arbitraty curve-fit of the form

$$\lambda = C(A_1 + (x/\theta)^2)^{1/6}/(x/\theta) \tag{3.3}$$

which has the asymptotic behaviour

$$\begin{aligned} \lambda &= CA_1^{1/6}/(x/\theta), \quad x/\theta \to 0, \\ &= C/(x/\theta)^{2/3}, \quad x/\theta \to \infty. \end{aligned} \tag{3.4}$$

The constants for this case were found to be $C \approx 2.67$ and $A_1 \approx 299$.

It should be noted that if the mean velocity excess does decay like $x^{-2/3}$ then the mean momentum equation implies that the spreading rate must scale with $x^{1/3}$. This spreading rate is also shown on log-log coordinates in figure 6.

It should be noted that for the purposes of these experiments the jet width is

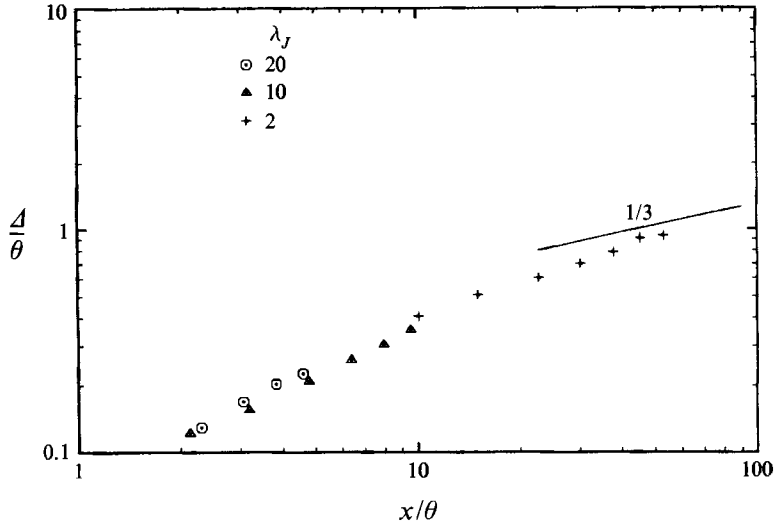

FIGURE 6. Growth of jet *vs.* x/θ on log-log coordinates showing 1/3 asymptote.

defined by

$$\Delta^2 = \left\{\int_0^\infty r^2(U - U_1)\mathrm{d}r\right\} \Big/ \left\{\int_0^\infty (U - U_1)\mathrm{d}r\right\}. \tag{3.5}$$

This follows Townsend (1976) and is based on the variance of the velocity distribution. As in the case of the decay of the centreline velocity excess, if it is assumed that far enough downstream the behaviour of the jet is determined only by the momentum excess, then the width of the jet is given by

$$\Delta/\theta = G[x/\theta]. \tag{3.6}$$

It may be seen in figure 6 that this equation is reasonably well satisfied by the results and an approach to a 1/3 power-law form is at least plausible.

3.2. *Mean velocity profiles*

Figure 7 shows the mean velocity profiles for the $\lambda_J = 10$ flow case at different streamwise stations. This case shows the typical collapse of the profiles when scaled with local parameters. Other cases show a similar collapse.

Figure 8 shows the profiles for all three coflow ratios at a single station ($x/D = 30$). Although the collapse here is not perfect it certainly shows that the functional form of the profiles for all three cases is quite close. Also shown on this figure is a curve-fit to the mean velocity profiles which is used later in the calculation of the Reynolds shear-stress from the mean flow parameters using the momentum equation.

3.3. *Reynolds Stress measurements*

In order to better describe and understand the Reynolds stress data it is useful to return to the concept of a flow which is independent of the exact initial conditions of its generation and depends only on the momentum imparted to it at its source. Thus the stresses may be considered to depend only on x/θ or equivalently on U_1/U_o (since if this argument holds it has already been shown that U_1/U_o is a universal function of x/θ). In this way the flow in the $\lambda_J = 2$ case for example may be treated as the far-downstream behaviour of the $\lambda_J = 10$ case. Thus rather than examining the

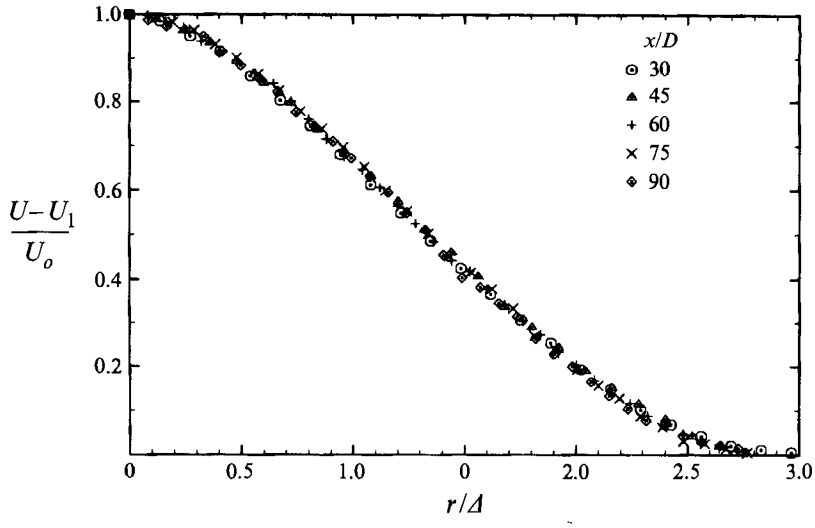

FIGURE 7. Mean velocity profiles for $\lambda_J = 10$.

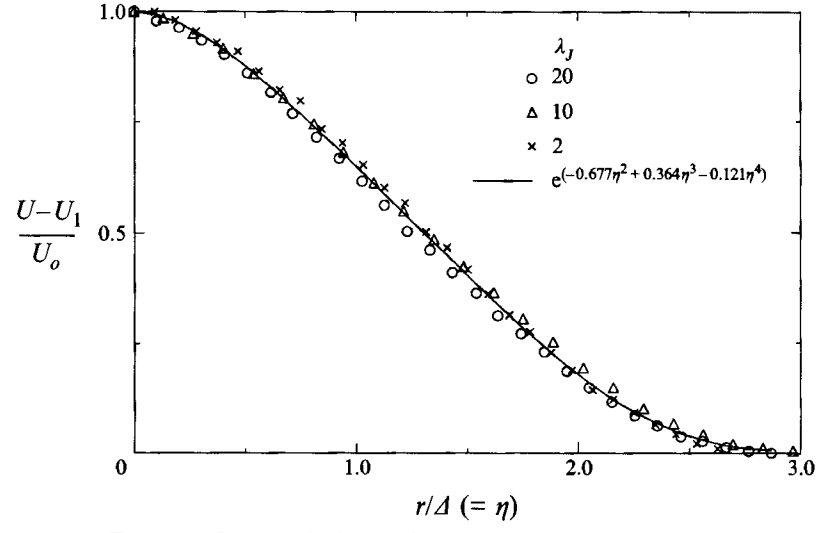

FIGURE 8. Mean velocity profiles at $x/D = 30$ for all three flow cases.

behaviour for three distinct flow cases it is possible to treat all the results as coming from one universal flow. Mathematically, then

$$\frac{\overline{u_i u_j}}{U_o^2} = F_{ij}\left[\frac{x}{\theta}, \frac{r}{\Delta}\right], \quad i,j = 1,2,3, \tag{3.7}$$

where the F_{ij} are universal functions of x/θ for a given r/Δ. In order to examine the behaviour of the Reynolds stresses a typical, or representative value is plotted *vs.* x/θ. For the normal stresses ($\overline{u^2}$, $\overline{v^2}$ and $\overline{w^2}$) this is chosen as the value at the centreline and since the flow is axisymmetric then $\overline{v^2} = \overline{w^2}$ on the centreline and hence only $\overline{w^2}$ is shown. Since the shear stress is zero on the centreline then the characteristic value for this component is chosen as the value of the maximum. The results are

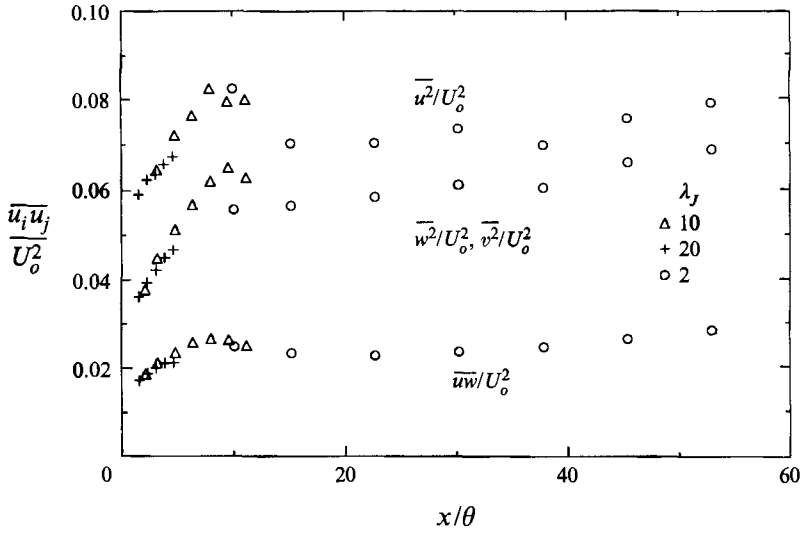

FIGURE 9. Variation of Reynolds stresses *vs.* x/θ.

shown in figure 9. The behaviour is very interesting. Although the higher coflow cases ($\lambda_J = 10, 20$) appear to collapse on a universal curve, there seems to be a slight drop in the level of the stresses for the $\lambda_J = 2$ case. This may be due to further differences in initial conditions in this case. Apart from this it would appear that all the stress components reach a peak at about $x/\theta = 9$, drop off to a broad minimum, then continue gradually to increase.

If the flow were to reach a self-preserving (or approximately self-preserving) state then the functions F_{ij} would be expected to become asymptotically constant (i.e. independent of x/θ). The results of Antonia & Bilger (1973), which extend beyond $x/\theta = 100$, show that the stresses appear to be increasing even at this distance. An important point to note when assessing these results is that the uncertainty in the non-dimensional stresses is significantly affected of the uncertainty in the measurement of the velocity excess.

Further information on the possible approach of axisymmetric flows to a self-preserving small-excess (or small-deficit in the case of wakes) state may be obtained by referring to table 1.

Some initial points should be noted. Firstly some of the results have been measured from plots of published data. While care was taken to make the measurements accurate there will inevitably be some error involved. Another point is that the values of the stresses given by Antonia & Bilger (1973) for their $\lambda_J = 2$ case seem to be much larger than the results of the present study and of the other coflowing jet studies shown at similar coflow ratios. The reason for this is not known.

It may be seen that the measured stresses for the wake flows (excluding Chevray 1968) are much larger than any of the measurements made in coflowing jets, suggesting that the turbulence is more significant in these flows. This may be related to the rather severe disturbances characteristic of the initial conditions in these flows. These initial disturbances die out rather slowly and so may affect the turbulence far downstream. It may be noted that the measured stresses are highest in the case of the wake of the disk but much lower in the case of the wake of a spheroid, a fact which is consistent with this explanation. This is also shown convincingly in the results

Author	Flow	x/D	$\overline{u^2}/U_o^2$	$\overline{uw}/U_o^2$	$\overline{u^2}/\overline{w^2}$	$\overline{u^2}/\overline{uw}_m$
Wygnanski & Fiedler (1969)	Free jet	90	0.078	0.016	1.28	4.6
Antonia & Bilger (1973)	Coflowing jet					
	λ_J =3.5	248	0.154	0.038	–	3.05
	λ_J =2	200	0.23	0.060	–	3.90
Biringen (1986)	Coflowing jet					
	λ_J=9	200	0.094	0.025	1.96	3.76
	λ_J=4	178	0.082	0.029	2.10	2.83
	λ_J=2.33	182	0.14	0.033	2.37	4.24
Smith & Hughes (1977)	Coflowing jet					
	λ_J=0.75	40	0.073	0.028	3.79	2.61
Present Study	Coflowing jet					
	λ_J=20	30	0.058	0.017	1.62	3.37
	λ_J=20	90	0.068	0.021	1.43	3.23
	λ_J=10	90	0.080	0.026	1.28	3.05
	λ_J=2	90	0.075	0.026	1.14	2.88
Uberoi & Freymuth (1970)	Wake of sphere	100	0.727	0.27	1.10	2.69
Chevray (1968)	Wake of spheroid	18	0.09	0.05	1.10	2.33
Carmody (1964)	Wake of disk	28	–	0.52	–	2.33
Bevilaqua & Lykoudis (1978)	Wake of sphere	110	0.447	–	–	–
	Wake of porous disk	110	0.0528	–	–	–

TABLE 1. Characteristic parameters of jet and wake flows. (D is nozzle exit diameter.)

of Bevilaqua & Lykoudis (1978) where the streamwise turbulence intensity is much higher for the wake of a sphere than for the wake of a porous plate with the same drag coefficient (which is comparable to the values recorded in coflowing jets). It is interesting that the ratio of streamwise turbulence intensity to radial turbulence intensity on the centreline is comparable in all flows and does not appear to be greatly affected by the initial conditions. It appears to approach one for the wake flows. The results of the present study also show a monotonic decrease toward the wake value as the flow changes from a free-jet-like state toward a small-excess-jet-like state. Unfortunately the results of Biringen (1986) show the opposite trend, i.e. this quantity increases as the coflow ratio is decreased. His results are also higher than those of the present study (and even higher than the results of Wygnanski & Fiedler 1969 for a free jet). It is possible that this is related to the initial conditions of the flow since the results of Smith & Hughes (1977) (who had initial conditions like a fully developed pipe flow with, most probably, significant external boundary layers as well) are even higher.

Also of interest is the ratio of the streamwise turbulence intensity to the Reynolds shear stress. The present results again show a monotonic decrease from the high values characteristic of a free jet (4.6 for Wygnanski & Fiedler 1969) to the lower values characteristic of the wake flows (about 2.3). Unfortunately here again the results of Biringen (1986) are in conflict with the present data, as are the results of Antonia & Bilger (1973) (for λ_J = 3.5). However, those of Smith & Hughes (1977) seem to support a trend toward smaller values as the coflow is increased. It is possible that Biringen (1986) may have had different initial conditions requiring the specification of other parameters in addition to λ_J for the three different flow cases reported.

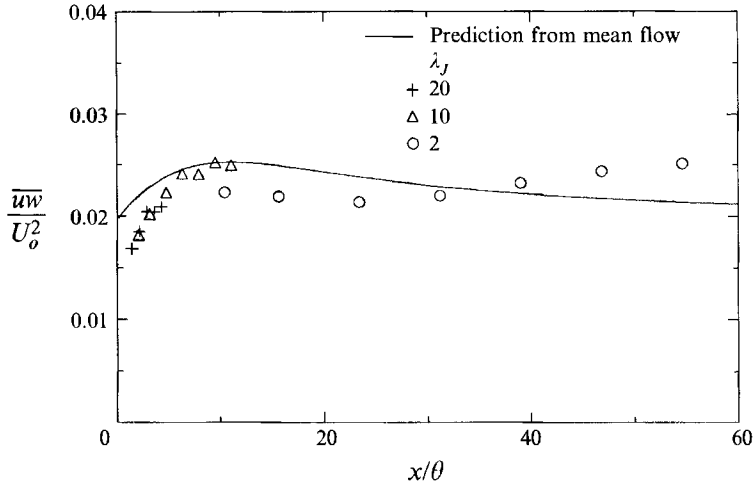

FIGURE 10. Comparison of prediction from (4.2) and the curve-fit to the mean velocity excess with the experimental results for the shear stress at $\eta = 1$.

4. Reynolds shear stress calculations

The momentum equation for axisymmetric flow is given by

$$U\frac{\partial U}{\partial x} + W\frac{\partial U}{\partial r} + \frac{\partial(\overline{u^2} - \overline{w^2})}{\partial x} = -\frac{1}{r}\frac{\partial(\overline{uw}r)}{\partial r}. \tag{4.1}$$

In this equation the viscous stresses have been neglected and small terms relating to gradients of the normal stresses have been dropped. If the normal stress terms are neglected then using this equation it is possible to calculate the Reynolds shear stress using only mean flow quantities. In particular, in the case of zero-pressure-gradient flow, it is possible to use the continuity equation and the momentum integral equation to eliminate the mean cross-stream velocity (W) and to express terms involving the jet radius (Δ) in terms of the non-dimensional velocity excess (λ). After some algebra this results in an expression for $\overline{uw}/U_o^2$ given by

$$\frac{\overline{uw}}{U_o^2} = -\frac{1}{\xi(2\pi)^{1/2}}\frac{1}{(I_1+\lambda I_2)^{3/2}}\frac{1}{\lambda^{5/2}}\frac{\partial\lambda}{\partial x^*}\left[\tfrac{1}{2}I_1\xi^2 f + \lambda(I_2\xi^2 f + I_1 I_B - I_A I_2) + \lambda^2 I_2 I_A f\right]. \tag{4.2}$$

Here $x^* = x/\theta$, $f = f[\xi] = (U - U_1)/U_o$, $\xi = r/\Delta$ and the I-terms are integrals of f given by

$$I_A = \int_0^\xi \xi f \mathrm{d}\xi, \quad I_B = \int_0^\xi \xi f^2 \mathrm{d}\xi, \quad I_1 = \int_0^\infty \xi f \mathrm{d}\xi, \quad I_2 = \int_0^\infty \xi f^2 \mathrm{d}\xi.$$

Hence we arrive at an equation for the Reynolds shear stress of the form

$$\overline{uw}/U_o^2 = g[\lambda, x/\theta, \xi]. \tag{4.3}$$

Then, using the curve-fit to the centreline velocity excess and the curve-fit to the mean velocity profiles, it is possible to express λ in terms of x/θ. Hence the Reynolds shear stress becomes a function only of x/θ for a given ξ (at least for a given flow where the curve-fit to the λ versus x/θ data applies).

Figure 10 shows the calculation of the Reynolds stress using this equation at $\xi = 1$ (which is close to the maximum Reynolds shear stress) compared with the experimental results.

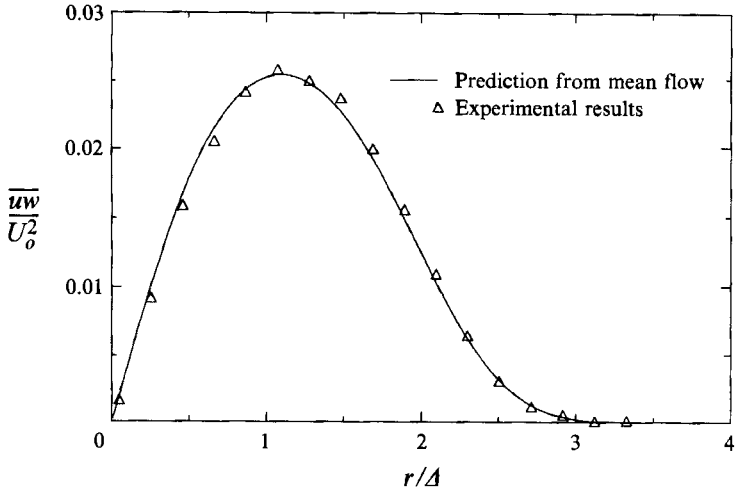

FIGURE 11. Comparison of prediction from (4.2) and the curve-fit to the mean velocity excess of the variation of the shear stress with cross-stream coordinate with the experimental results ($\lambda_J = 10$, $x/D = 90$, $x/\theta = 9$).

The calculation seems to give the correct trends except at very large x/θ where the experimental data continue to increase while the prediction appears to approach an asymptotic value. The quantitative agreement is not perfect, but is encouraging. This is perhaps not surprising given that the normal stress terms have been neglected and that the curve-fit is not perfect (particularly when finding derivatives). These effects may explain the departure at small x/θ. The departure at large (x/θ) is more serious and cannot be explained in terms of the neglected stresses or the nature of the curve-fit.

At this stage the reason for the departure is not known, but it is possible that the wind-tunnel walls have some effect on the axisymmetry of the flow at these far stations. It should also be noted that for the $\lambda_J = 2$ case there appears to be a departure from the 'universal' curve mentioned earlier which may be due to the small difference in the initial conditions. Based on the earlier discussion it would seem that less severe initial disturbances lead to smaller values of stresses. In the $\lambda_J = 2$ case the initial profile is not quite a top-hat shape and has smaller mean velocity gradients. This effect needs to be examined further before any firm conclusions can be made. It suggests that, perhaps, the Reynolds stresses also depend on some parameter related to the severity of the initial disturbance. In order to examine the agreement of the variation of shear stress with $\xi = r/\Delta$ the station at $x/\theta = 9$ was chosen since the agreement of magnitudes here is good (see figure 10). Figure 11 shows the excellent agreement of the functional form for this station.

4.1. *A note on prediction of the evolution of the coflowing jet*

In order to calculate the evolution of the axisymmetric jet (i.e. the variation of jet diameter and decay of the centreline velocity excess) it is necessary to make some extra assumptions about the behaviour of the mean quantities. The momentum integral equation relates the growth of the jet to the decay of the centreline mean velocity but this is not sufficient to give the growth as a function of streamwise distance. To find the evolution it is necessary to solve for two quantities, the local jet diameter and the local velocity excess. Use of the momentum integral equation eliminates one

quantity and reduces the problem to one of solving for one parameter. One form of this parameter as given by Townsend (1976) is the entrainment parameter which may be written as

$$\beta = \frac{1 + \frac{1}{2}\lambda}{|\lambda|}\frac{\mathrm{d}\Delta}{\mathrm{d}x} \tag{4.4}$$

and is constant for any one type of self-preserving flow but varies between different types of self-preserving flow. In the case of a non-self-preserving flow like the coflowing jet this parameter varies with streamwise distance from a value approaching that of a self-preserving free jet to that approaching a self-preserving small-excess jet. Some calculations of the evolution of the coflowing jet have been based on the assumption of geometrical similarity of the Reynolds stresses with a local velocity scale which is not equal to the local velocity excess but varies with streamwise distance (e.g. see Bilger 1968; Antonia & Bilger 1973; Townsend 1976, pp. 255–258). Use of the energy integral equation then makes it possible to solve for the streamwise evolution of the entrainment parameter. Consideration of the asymptotic forms of (4.2), however, shows that the functional form for the shear stress is different in the case approaching a jet exhausting into still air ($\overline{uw}/U_o^2 \sim I_A f/\xi$) and in the case of a small-excess jet ($\overline{uw}/U_o^2 \sim \xi f$). Figure 12(*a*) shows these two forms scaled to have the same magnitude. It may be seen that the geometrical forms are quite different and hence this method cannot be applied over the whole range of the flow. Of course (4.2) neglects the variation of the normal stresses so in order to check that this change of shape occurs in the real flow, figure 12(*b*) shows two profiles for stations close to the two asymptotic limits. It would seem then that the variation in shape predicted by (4.2) also occurs in the experiment. This may explain why Antonia & Bilger (1973) could not find real solutions for the entrainment parameter with this approach (assuming geometrical similarity of the Reynolds stresses) using any reasonable experimental inputs.

5. Reynolds number effects in the flows studied

With the aid of equation (4.2), in conjunction with (3.3) and the curve-fit to the mean velocity profile shown in figure 8, the ratio of the Reynolds shear stress to the viscous shear stress can be computed (i.e. $\overline{uw}/(\nu\partial U/\partial r)$ and was evaluated at $\xi = 1$ which is close to the point of maximum Reynolds shear stress). In the cases reported, this varies from 500 to 3000 so one would expect Reynolds number similarity in the sense of Townsend (1976) to apply, i.e. the mean relative motions and the energy-containing motions should be independent of viscosity. The same could be said of all the other flow cases shown in table 1.

6. Spectra

6.1. *The high-wavenumber motions*

Kolmogorov scaling

According to Kolmogorov (1941) as the energy of the flow is transferred from large to smaller eddies the overall processes determining the flow become progressively less organized. If the Reynolds number of the flow is high enough then the smallest eddies should be isotropic and their energy should be determined by viscosity and turbulent dissipation alone. This leads to the definition of the Kolmogorov length and velocity

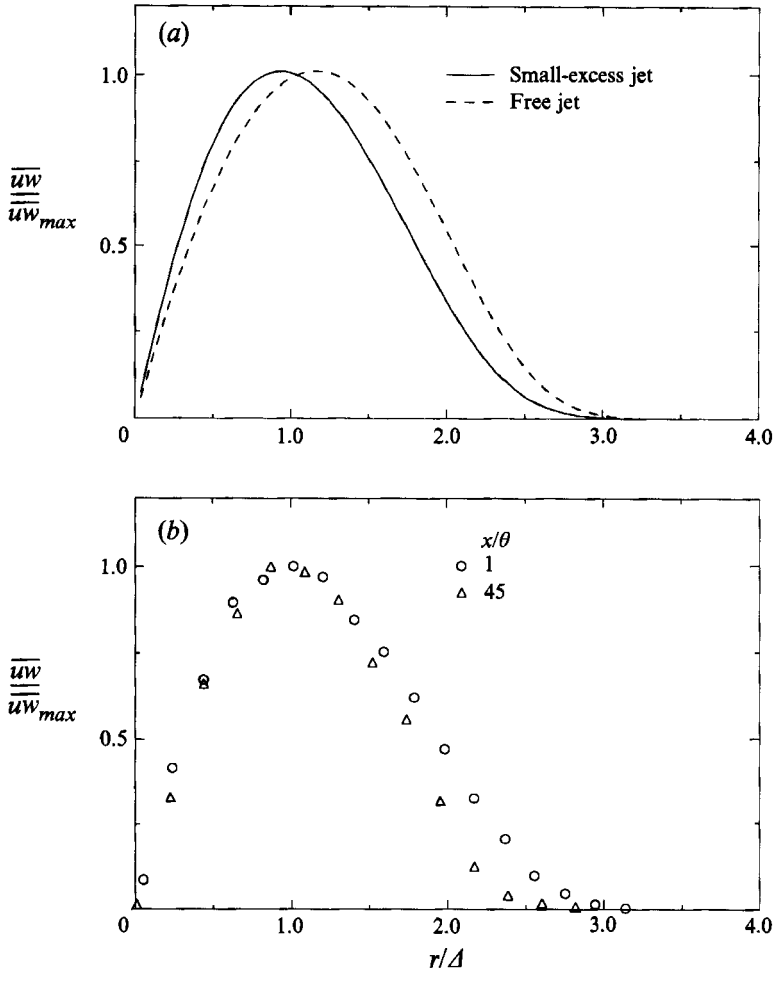

FIGURE 12. (*a*) Comparison of the asymptotic functional forms for the shear stress of (4.2). The curves have been scaled to have the same maximum value. (*b*) Comparison of the functional forms of the experimental data for two stations, one approaching a free jet and the other approaching a small-excess jet state.

scales:

$$\eta = \left(\frac{\nu^3}{\epsilon}\right)^{1/4} \tag{6.1}$$

and

$$\upsilon = (\nu\epsilon)^{1/4}. \tag{6.2}$$

In order to calculate these scales it is necessary to estimate the dissipation. Here the isotropic assumption was used to estimate the dissipation from the stream wise spectra:

$$\epsilon = 15\nu\overline{\left(\frac{\partial u}{\partial x}\right)^2}. \tag{6.3}$$

Application of Taylor's hypothesis makes it possible to estimate $\partial u/\partial x$ in terms of

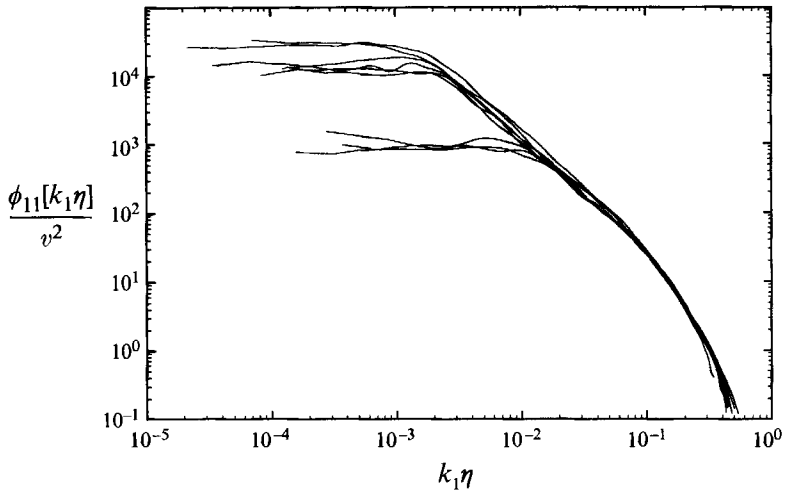

FIGURE 13. Streamwise spectra for all stations at $r/\Delta = 1$.

$\partial u/\partial t$ and transforming to wavenumber space (6.3) becomes

$$\epsilon = 15\nu \int_0^\infty k_1^2 \phi_{11}[k_1] \mathrm{d}k_1 \tag{6.4}$$

Figure 13 shows one profile from each of the streamwise stations measured for all three flow cases plotted on a single set of axes at r/Δ=1 which is close to the point of maximum shear stress. Plotting these results is a good test for the applicability of this scaling since the Kolmogorov scales vary significantly between flow cases (the dissipation varies by a factor of approximately 2000 over this range so the length and velocity scales vary by a factor of approximately 6.5). It may be seen that all profiles seem to collapse at the high-wavenumber end of the spectra. Hence these results show that the high-wavenumber collapse occurs for all flow cases regardless of the local Reynolds number or the Reynolds shear stress. It should be noted that a similar collapse occurs for the other normal components of spectra which are not shown here.

It is interesting to observe the peel-off that occurs from the $-5/3$ law as the Reynolds number decreases. Figure 14 shows this trend. Three stations are shown from each flow case and the spectrum is premultiplied by $(k_1\eta)^{5/3}$ so that a $-5/3$ law corresponds to a plateau. It may be noted that the high-wavenumber end appears universal and the different flow cases peel-off from a $-5/3$ law at the low-wavenumber end. The Taylor microscale Reynolds number, R_λ, drops from 434 to 84 in this plot. Here the Taylor microscale is defined as

$$\lambda_T^2 = \frac{\overline{u^2}}{\overline{(\partial u/\partial x)^2}} \tag{6.5}$$

and was calculated using the isotropic assumption, i.e.

$$\lambda_T^2 = 15\nu \frac{\overline{u^2}}{\epsilon} \tag{6.6}$$

(where ϵ is the dissipation).

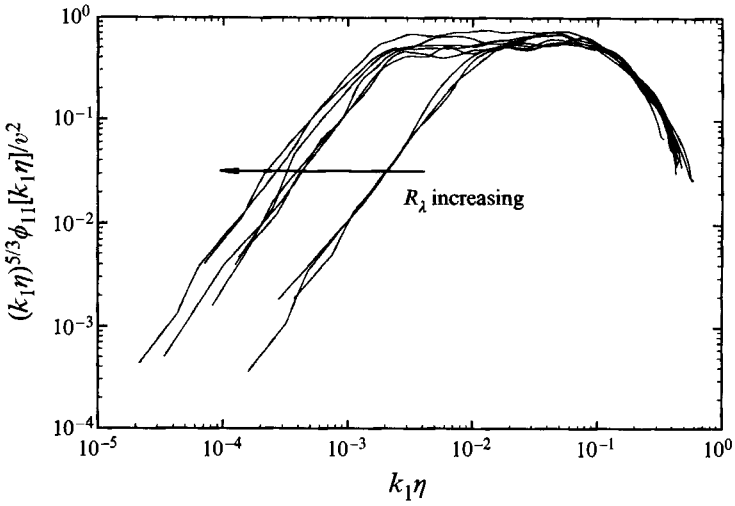

FIGURE 14. Peel-off from $-5/3$ law with decreasing Reynolds number.

It should be pointed out that the meaning of the Taylor microscale is not clear in a turbulent shear flow since it is really a concept that only applies to isotropic turbulence. It is mentioned here only as a basis for comparison and since it is used by many authors as the appropriate Reynolds number when considering fine-scale motions. The peel-off at the highest wavenumbers can be shown to be due to the spatial resolution of the hot-wire probes and varies due to the variation of η and hence ℓ/η where ℓ is the length of the hot-wire sensor (this peel-off occurs where $k_1\ell = 1$ for each profile).

6.2. *Isotropy and the $-5/3$ law*

The spectra in the high-coflow ratio case shows distinct regions which may be interpreted as corresponding to a $-5/3$ law. This is not surprising since this flow case approaches that of a free jet, for which other researchers have observed similar behaviour (see Gibson 1963). The $-5/3$ law is traditionally associated with the concept of local isotropy, as originally proposed by Kolmogorov (1941). In order to examine the relationship between the $-5/3$ law observed in this flow case and the concept of local isotropy measurements of the spectral Reynolds shear stress correlation coefficient were made for flow cases that exhibited a $-5/3$ law. This also gives some information about the structure of the flow since it shows at which scales the Reynolds shear stress is produced. The spectral Reynolds shear stress correlation coefficient will be defined here as

$$R_{13}[k_1\eta] = -\frac{\phi_{13}[k_1\eta]}{(\phi_{11}[k_1\eta]\phi_{33}[k_1\eta])^{1/2}}. \tag{6.7}$$

If the flow is isotropic at some point in wavenumber space then this quantity should be zero. Figure 15 shows the streamwise spectrum premultiplied by $(k_1\eta)^{5/3}$ and the plateau corresponds with an inertial subrange. Also shown on the same plot is the correlation coefficient spectrum. The correlation coefficient R_{13} can be seen to be finite but drops rapidly to small values at the high end of the wavenumber scale. The negative values at high wavenumbers were initially thought to be due to correlated electronic noise on the signals; however some results from the model to be

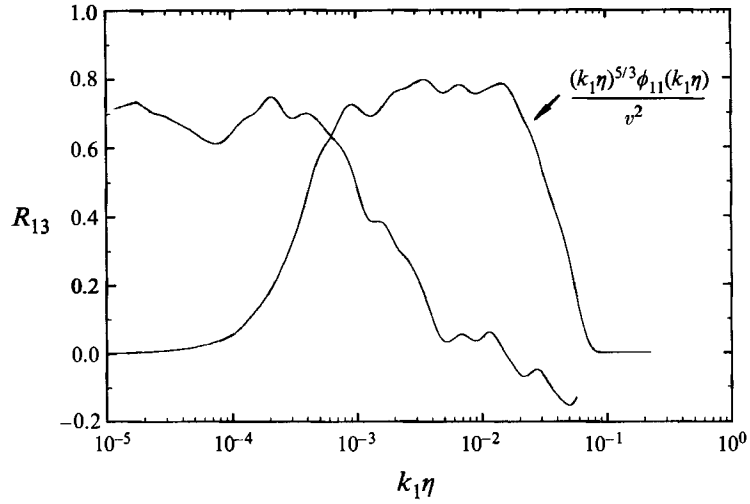

FIGURE 15. Reynolds shear stress correlation coefficient at $x/D = 30$ for $\lambda_J = 20$ and $r/\Delta = 1$ ($R_\lambda = 434$). This plot also shows the streamwise spectrum premultiplied by $(k_1\eta)^{5/3}$.

presented later suggest that these may in fact be a characteristic of the structure of the large-scale energy-containing eddies. Since a given eddy may have energy spread over a range of wavenumbers, the finite R_{13} in the plateau region is probably coming from contamination of this region from the signatures of the large scales whereas the fine-scale eddies in the plateau region are probably isotropic, although there is no way of proving this at this stage. Some results of the model presented later support this idea of contributions to the high wavenumbers from the large scales.

6.3. *Structure of the flow*

In order to examine the distribution of energy in wavenumber space it is useful to examine the form of the premultiplied spectra (i.e. $k_1\Delta\phi_{ij}[k_1\Delta]/U_o^2$) plotted versus $\log[k_1\Delta]$. In this form, the area under the graph is the contribution to the appropriate component of the Reynolds shear stress tensor. Particularly useful are the cospectra since these will depend on the large scales in the flow and should be uncontaminated by the small-scale locally isotropic eddies mentioned in the previous section. In order to examine the distribution of the stresses in wavenumber space we will consider here the spectra normalized by their maximum values so that we may examine changes in bandwidth with Reynolds number and position without regard to the changes in magnitude which must occur due to the nature of the flow. Figure 16 shows the variation of $k_1\Delta\phi_{13}[k_1\Delta]$ with changes in local Reynolds number ($R_\Delta = U_o\Delta/\nu$) at a fixed $r/\Delta = 1$. It may be seen that there is little variation in the bandwidth, which suggests that the structure is unaffected by Reynolds number. This is in line with Townsend's (1976) Reynolds number similarity hypothesis.

Hence the large-scale structure is seen to be Reynolds number invariant. It is also interesting to note that all of the contributions to the cospectra occur in a band centred on $k_1\Delta = 1$, which extends approximately from $k_1\Delta = 0.1$ to $k_1\Delta = 10$, which suggests that the eddies contribute to the Reynolds shear stress are of a size of order Δ.

Figure 17 shows the variation of the cospectra with non-dimensional cross-stream coordinate r/Δ. It may be seen that there is little variation, suggesting that the distribution of eddies does not change with cross-stream position. The appropriate

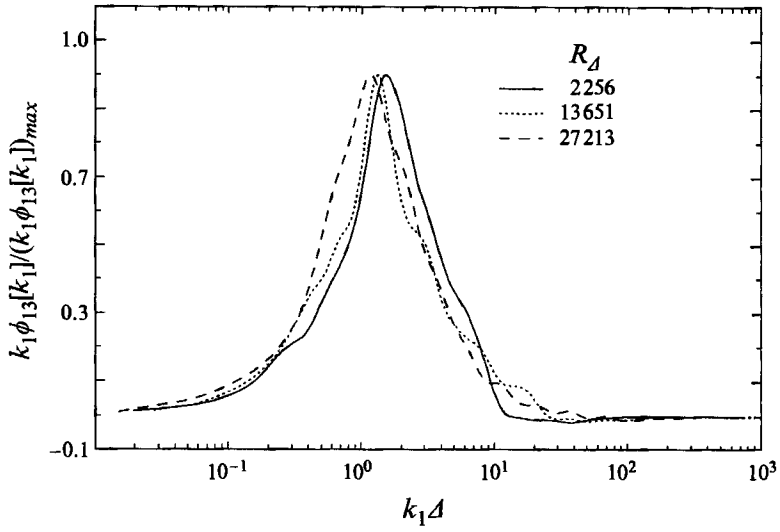

FIGURE 16. Variation of bandwidth of cospectra with Reynolds number at fixed $\eta = 1$.

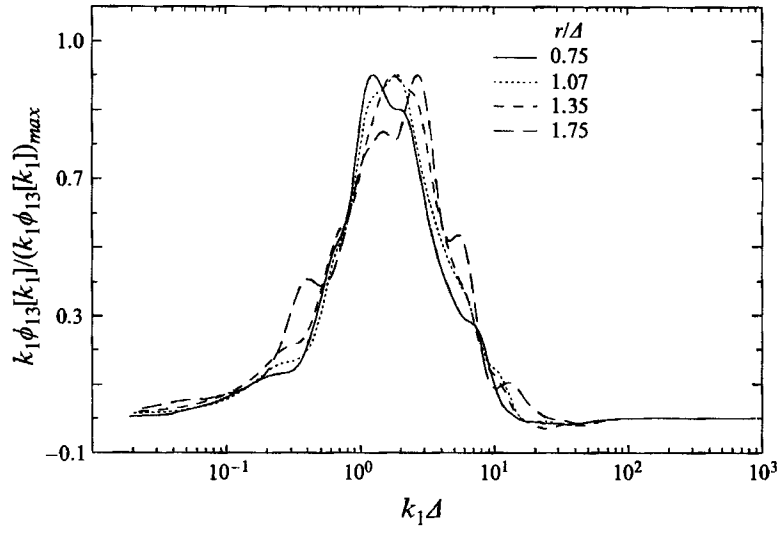

FIGURE 17. Variation of bandwidth of cospectra with cross-stream position (r/Δ).

length scale is the local jet width regardless of position. This suggests that the bandwidth is independent of cross-stream position, in contrast to boundary layers where recent results (Marušić, Nickels & Perry 1994) have shown that the bandwidth of the Reynolds stress increases as the wall is approached (a fact which is consistent with the model of Perry & Chong 1982).

These results suggest that the Reynolds shear stress in jets is produced by eddies of a size which scales with the local jet radius and which span the jet radius. For comparison with figure 16, and in order to show the effect of the fine scales or 'isotropic' motions, figure 18 shows the streamwise component of the spectra pre-multipied by $k_1\Delta$ and divided by its maximum value for two extreme values of R_Δ. It can be seen that there is an increase in the high-wavenumber energy with the increase in R_Δ which is not present in the cospectra. At this point it is speculated that this

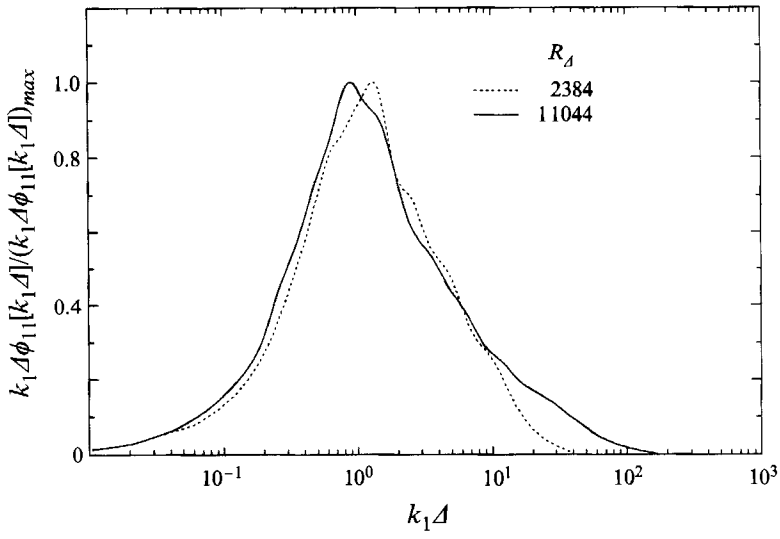

FIGURE 18. Variation of bandwidth of streamwise spectra with Reynolds number.

comes from fine-scale isotropic eddies which scale with the Kolmogorov length and velocity scales.

7. A model for axisymmetric turbulent jets

It has been suggested by Townsend (1976) based on a study of correlation measurements that the main turbulent motion in turbulent free shear flows is probably dominated by double-roller eddies which are inclined to the streamwise direction. The characteristic velocity scale of these coherent structures is proportional to U_o and the characteristic length scale is of order Δ, the characteristic jet radius. They probably carry most of the Reynolds shear stress and each double roller-eddy has a limited azimuthal extent. Such structures are consistent with the experimental observations of Dahm & Dimotakis (1986) and Shlien (1987). Figure 19 illustrates a suggestion for such a structure and it is envisaged that a number of these structures are arranged randomly in different azimuthal and streamwise positions with equal probability. The overall shape of the structure was suggested in part by the experiments of Liepmann & Gharib (1992) and the vortex calculations of Martin & Meiburg (1991). The dimensions shown in figure 19 are for one particular test structure which has been used to compute the results which follow. The aim is to see if the mean flow distribution, the energy-containing Reynolds stress distributions and the associated spectra are consistent with such a model. An analysis will be developed here which is somewhat analogous to that developed by Perry & Chong (1982) and Perry, Henbest & Chong (1986) for the random distribution of horse-shoe structures in a turbulent boundary layer. The test-case eddy structure is composed of straight vortex rods to simplify the analysis and these rods have been given a Gaussian distribution of vorticity to avoid singularities in the velocity field. It is also envisaged that these structures are immersed in a *sea* of fine-scale turbulence which is probably locally isotropic. In the model this background turbulence is not included and hence we would expect some energy to be missing at the high-wavenumber end of the spectra.

The analysis is as follows. From the Biot-Savart law, for a given structure, the

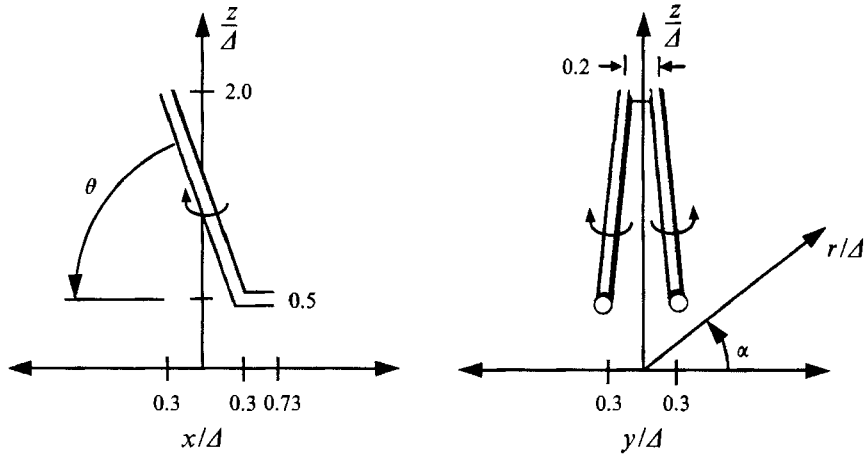

FIGURE 19. Eddy structure used in the model.

velocity due to a single structure is

$$\frac{u_i}{U_e} = f_i[\hat{x}, \hat{y}, \hat{z}] \tag{7.1}$$

where U_e is the characteristic velocity of the eddy (which will be proportional to Γ/Δ, where Γ is the circulation of the eddy used) and the $\hat{}$ denotes a length non-dimensionalized by Δ (e.g. $\hat{x} = x/\Delta$). Taking Fourier transforms (FFTs are used in the numerical work) of the velocity signatures along lines in the streamwise direction gives

$$F_i[k_1\Delta, \hat{y}, \hat{z}] = \int_{-\infty}^{\infty} f_i[\hat{x}, \hat{y}, \hat{z}] e^{-j2\pi k_1 \Delta \hat{x}} d\hat{x} \tag{7.2}$$

where k_1 is the streamwise wavenumber and $j = \sqrt{-1}$. The contribution to the power spectral density for each streamwise cut from one eddy structure is

$$p_{ij}[k_1\Delta, \hat{y}, \hat{z}] = \mathrm{Re}\{F_i^*[k_1\Delta, \hat{y}, \hat{z}] F_j[k_1\Delta, \hat{y}, \hat{z}]\} \tag{7.3}$$

where Re denotes the real part of a complex function and * denotes the complex conjugate. For a given short section of jet there probably exist many such eddies arranged at different azimuthal locations (different α) perhaps in a star-shaped array. Since the eddies exist in an unbounded fluid they can also move randomly in the vertical and horizontal directions (i.e. the y- and z-directions), although we would expect this movement to be bounded (otherwise the jet would have infinite extent). In this analysis this random freedom of movement is accounted for by jittering a single eddy bodily in both the horizontal and vertical directions. This idea is consistent with the observations of intermittency of the turbulence at the edge of a turbulent shear flow. In this analysis a Gaussian jitter is applied to the simple eddy using the following convolution integral:

$$\tilde{p}_{ij}[k_1\Delta, \hat{y}, \hat{z}] = \frac{(ab)^{1/2}}{\pi} \int_{-\infty}^{\infty} \int_{-\infty}^{\infty} p_{ij}[k_1\Delta, (\hat{y} - \hat{\chi}), (\hat{z} - \hat{\zeta})] e^{-(a\hat{\chi}^2 + b\hat{\zeta}^2)^2} d\hat{\chi} d\hat{\zeta}. \tag{7.4}$$

The tilde denotes a jittered function, $\hat{\chi}$ and $\hat{\zeta}$ are the non-dimensional shifts in the y- and z-directions respectively and a and b will be referred to as the (non-dimensional) jitter parameters. In this study a and b are assumed to be equal for simplicity.

A new stress function may be formed using the following transformation (presented in tensor notation):

$$\tilde{q}_{ij}(k_1, r, \phi) = R_{pi} R_{qj} \tilde{p}_{pq}(k_1, r\cos\alpha, r\sin\alpha) \tag{7.5}$$

where R_{ij} is the rotation tensor which represents rotation about the x-axis which may be written in a matrix form as

$$R_{ij} = \begin{bmatrix} 1 & 0 & 0 \\ 0 & \cos\alpha & \sin\alpha \\ 0 & -\sin\alpha & \cos\alpha \end{bmatrix} \tag{7.6}$$

In the numerical scheme the rotated spectral components are calculated first at points on the original Cartesian grid using (7.5) and then the values are interpolated onto a new cylindrical grid with similar resolution.

To find the (cross) power spectral density we average this spectral function for all streamwise cuts for different α and multiply by the eddy density:

$$\phi_{ij}[k_1\Delta, \hat{r}] = \frac{N}{2\pi}\int_0^{2\pi} \tilde{q}_{ij}[k_1\Delta, \hat{r}, \alpha]\mathrm{d}\alpha \tag{7.7}$$

where N is the average number of eddies per unit streamwise distance and per unit revolution in α. The Reynolds stresses are then calculated by integrating the appropriate power spectral densities thus:

$$\frac{\overline{u_i u_j}[\hat{r}]}{U_e^2} = \int_{-\infty}^{\infty} \phi_{ij}[k_1\Delta, \hat{r}]\mathrm{d}k_1\Delta. \tag{7.8}$$

The mean velocity can be found as follows. The contribution to the mean velocity from one eddy is

$$U[\hat{y}, \hat{z}] = \int_{-\infty}^{\infty} u_1[\hat{x}, \hat{y}, \hat{z}]\mathrm{d}\hat{x} \tag{7.9}$$

where u_1 is streamwise component of the Biot-Savart signature. From a single jittered eddy the contribution is

$$\tilde{U}[\hat{y}, \hat{z}] = \frac{(ab)^{1/2}}{2\pi}\int_{-\infty}^{\infty}\int_{-\infty}^{\infty} U[\hat{y} - \hat{\chi}, \hat{z} - \hat{\zeta}]\mathrm{e}^{-(a\hat{\chi}^2 + b\hat{\zeta}^2)^2}\mathrm{d}\hat{\chi}\mathrm{d}\hat{\zeta}. \tag{7.10}$$

Transforming to cylindrical coordinates we have

$$\tilde{U}_a[r, \alpha] = \tilde{U}[\hat{y}, \hat{z}] \tag{7.11}$$

where the subscript a refers to the function transformed to axisymmetric coordinates. Averaging over all signatures azimuthally and taking into account all eddies gives

$$\frac{\tilde{U}_a[\hat{r}]}{U_e} = \frac{N}{2\pi U_e}\int_0^{2\pi} \tilde{U}_a[\hat{r}, \alpha]\mathrm{d}\alpha \tag{7.12}$$

where U_a is the mean velocity and N is again the average number of eddies per unit streamwise distance and per unit revolution of α.

If we then non-dimensionalize the Reynolds stresses by the computed mean we find that the non-dimensional Reynolds stresses are premultiplied by $1/N$ since the stresses scale with N and the mean velocity squared depends on N^2. Hence there is an unknown scaling factor which depends on the density of the eddies in the sampling

volume. Here this factor is found by comparing the value of $\overline{u^2}/U_o^2$ at the jet axis and scaling all computed values by this one factor. In the case of the mean velocity distribution all values are scaled by the mean velocity excess on the jet axis as in experiment.

To obtain a rough guide as to the value of the jitter parameter a, intermittency measurements are useful. Corrsin & Kistler (1955) found that the position of the turbulent/non-turbulent interface given by $\hat{\zeta}[x,r,t]$ has a probability distribution

$$P[\zeta] = (2\pi\sigma^2)^{-1/2}\exp(-\tfrac{1}{2}(\zeta-\zeta_o)^2/\sigma^2) \tag{7.13}$$

(see Townsend 1976). Then it follows that the intermittency is

$$\gamma[X,r] = \int_r^\infty P[\zeta,X]\mathrm{d}\zeta. \tag{7.14}$$

If we take the top of the eddy as the position of the interface then for the eddy given $\zeta_o = 2\Delta$ (see figure 19), and the value of the jitter parameter used here ($a = b = 1.8$) gives $\sigma/\zeta_o \approx 0.26$ which is in reasonable agreement with experimental measurements for axisymmetric turbulent jets (estimates from the data of Wygnanski & Fiedler 1969 in a free jet give $\zeta_o = 2.2\Delta$ and $\sigma/\zeta_o = 0.22$).

8. Results

Results are compared with the experimental case for $x/D = 30$ and $\lambda_J = 2$. Many different eddy shapes have been tried as the representative double roller eddy but the one shown in figure 19 was chosen since it gave the correct Reynolds stress ratios and reasonably good shapes for the spectra. This does not necessarily mean that this is the final shape. It is best regarded as a 'first stab' which is consistent with the data. Exploring all possible shapes would be a major task. It will be noticed that two 'tail-pieces' have been added which aided in obtaining the correct stress ratios. Their form is similar to the streamwise vorticies found in both experiment (Liepmann & Gharib 1992) and in the numerical simulation of Brancher, Chomaz & Huerre (1994) which occur between distorted (star-shaped) ring vorticies in the near field of round jets. One point which may concern some readers is that the rods end in mid-air which means that the vorticity field is not divergence free. While this is not ideal it is simply an expedient to avoid the huge computational effort involved with generating an array of randomly distorted, and positioned, star-shaped vorticies. It should also be pointed out that while the vorticity field is not divergence free the velocity field is since it is, effectively, the curl of a stream function (see Winckelmans & Leonard 1993).

The results for the Reynolds stresses calculated for this structure are shown in figure 20 compared with experiment. Both the shapes and relative magnitudes of the stresses compare reasonably well with the experiment. The mean velocity profile generated by this structure is shown in figure 21 compared with experiment. In this case the agreement is reasonable. Figures 22–24 show the comparison of the computed spectra with the experimental data. It may be seen immediately that the model spectra drop off more quickly at high wavenumbers than the experimental data, a fact which may be attributed to the neglect of the fine-scale structure. The qualitative trends for the low-wavenumber region of the spectra are better. The cross-stream (ϕ_{22}) and radial (ϕ_{33}) spectra show a distinct 'bump' close to $k_1\Delta = 1$ in both the experiments and the model. This 'bump' is absent in the streamwise and Reynolds shear stress spectra, again for both the experiment and model. The position of the

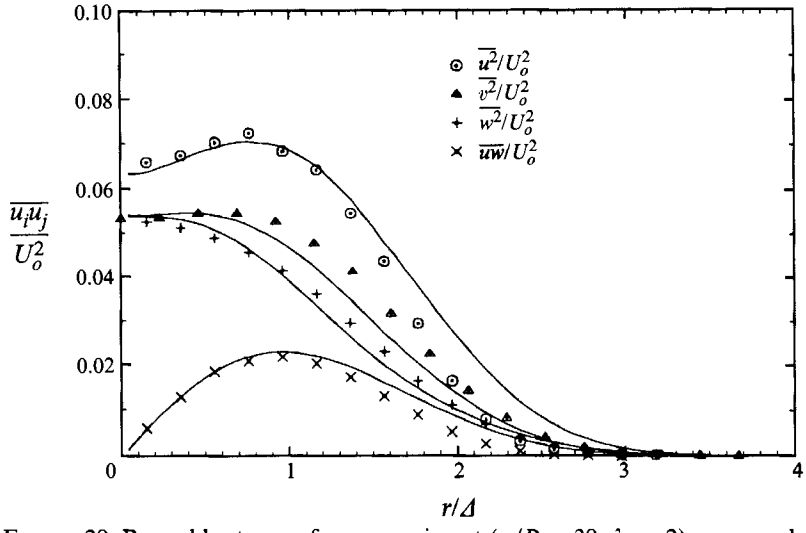

FIGURE 20. Reynolds stresses from experiment ($x/D = 30$, $\lambda_J = 2$) compared with model (solid lines).

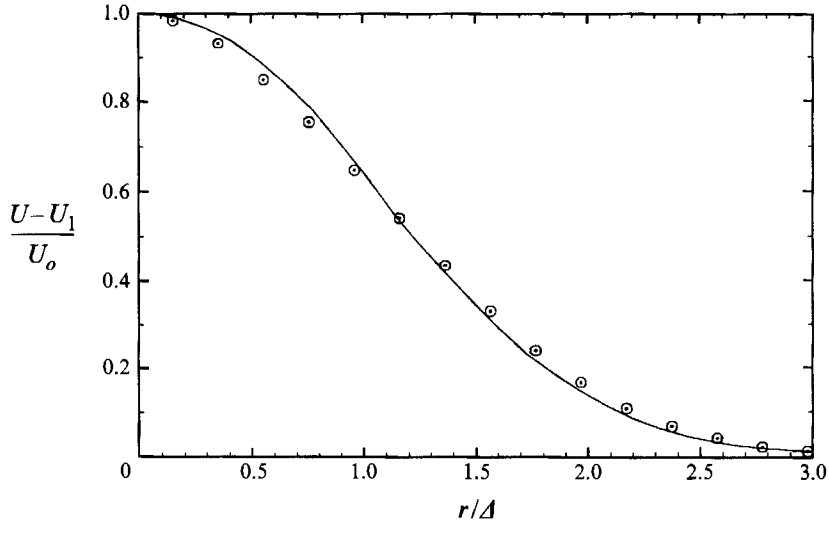

FIGURE 21. Experimental mean velocity profile ($x/D = 30, \lambda_J = 2$) compared with model (solid line).

'bump' and its shape and magnitude are not reproduced exactly. Another important difference between the ϕ_{22} and ϕ_{33} spectra from the model and experiment is that this 'bump' appears to be significant for all radial position in the experimental results but is only significant at large r in the model. This problem should hopefully be able to be overcome by modifying the details of the eddy structure. Also shown is the Reynolds shear stress correlation coefficient spectra calculated from both the model and experiment. The similarity is interesting. The comparison supports comments made earlier that the large-scale structures in the flow make significant contributions to the correlation coefficient even at high wavenumbers, but of course the contribution to the stresses at high wavenumber is negligible. Also of interest is that the model

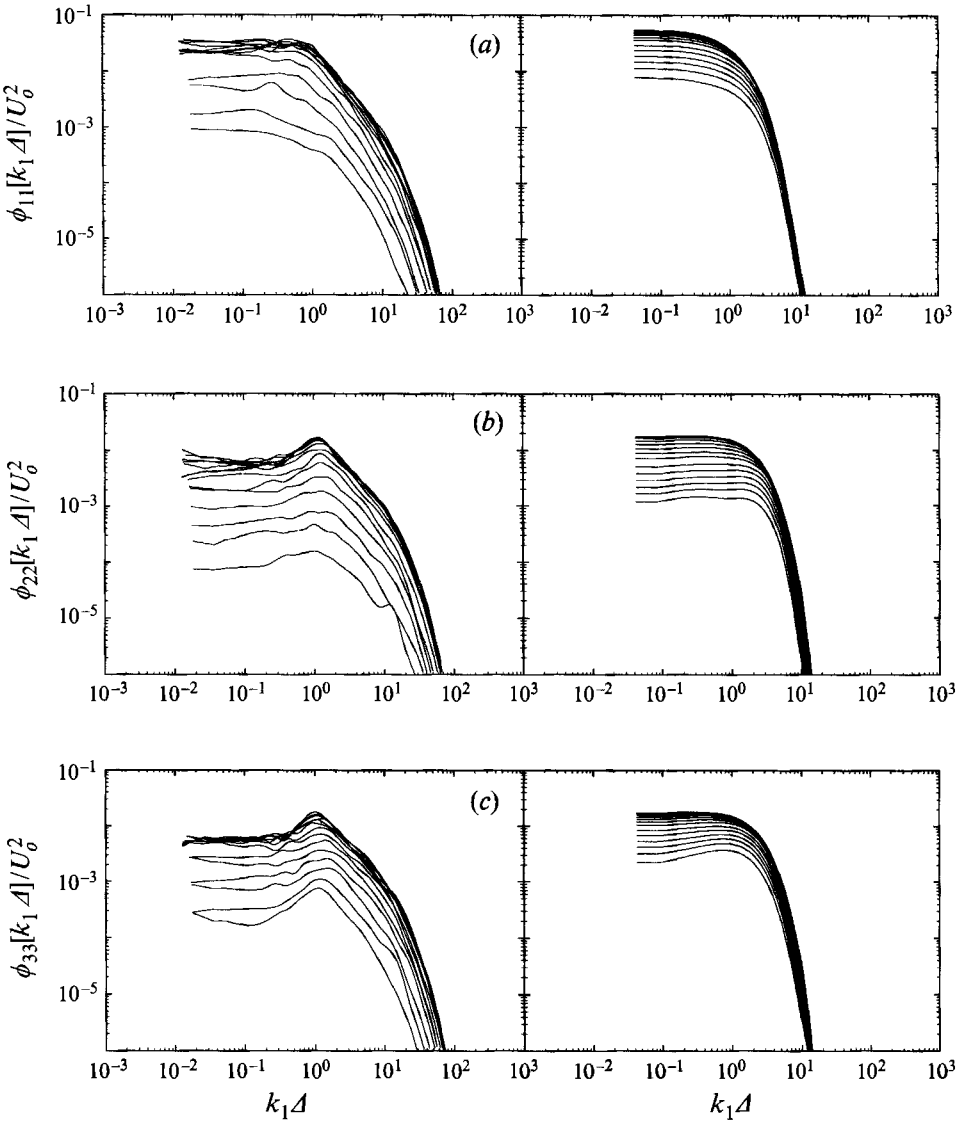

FIGURE 22. (*a*) Experimental streamwise spectra, (*b*) experimental cross-stream spectra, and (*c*) experimental radial spectra ($x/D = 30$, $\lambda_J = 2$, left) compared with model (right).

shows negative values for this quantity at high wavenumbers which also appear in experiment. The reason for this is not yet fully understood; however it suggests that this result in the experiments may not be due to correlated noise on the signals (further tests have shown that the noise is not large enough to explain the values). Extensive numerical tests also suggest that it is not due to aliasing or resolution problems in the model. Further investigation into this phenomenon is being carried out. It should be pointed out that this comparison was made for interest after the details of the model were fixed and the results had been calculated. No adjustments were made to improve the agreement for this quantity and the good agreement with experiment came as somewhat of a surprise to the authors.

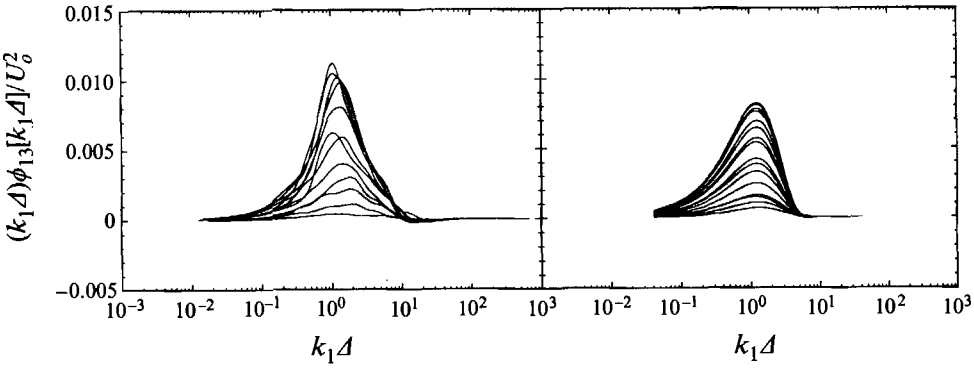

FIGURE 23. Experimental Reynolds shear-stress spectra ($x/D = 30$, $\lambda_J = 2$, left) compared with model (right).

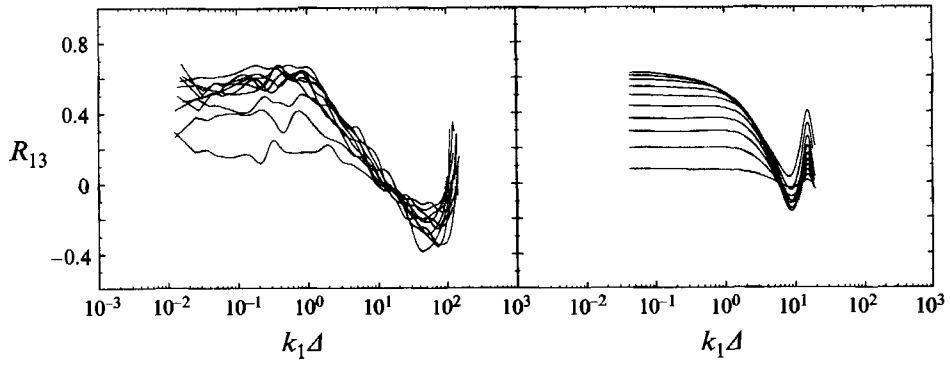

FIGURE 24. Experimental Reynolds shear-stress correlation coefficient spectra ($x/D = 30$, $\lambda_J = 2$, left) compared with model (right).

9. Discussion and conclusions

The experimental results presented show that with careful control of initial conditions different coflowing jet flows can be considered to be features of a single coflowing jet flow which depends on local conditions alone. The results also give a picture of the structure of the jet as consisting of some form of large-scale structure, which scales with the local jet width, that is responsible for a large part of the Reynolds shear stresses. In addition, the results suggest some additional fine-scale contributions to the normal components of the Reynolds stresses which may be isotropic and seem to scale with the Kolmogorov length and velocity scales.

Based on these observations a simple, crude model of an axisymmetric jet has been proposed. Whilst it is crude, it nevertheless predicts the correct qualitative trends for the radial profiles of Reynolds stresses, the mean velocity profiles, and even reproduces some features of the low-wavenumber spectrum and intermittency. It also shows some surprising results for the Reynolds shear stress correlation coefficient which also agree with experiment. Thus it shows sufficient promise to, at least, warrant further investigation. In order to improve the model further, the effects of changes in the large-scale structure need to be investigated in more detail including the effect of core size and orientation. These changes in structure may be able to be related to changes in the stresses as the flow changes from a free-jet-like flow to a small-excess jet flow.

The proposed model demonstrates several of the qualitative trends exhibited by experimental measurements in jets. Further work needs to be done to justify the underlying assumptions inherent in the model and to investigate its relationship to the real structure of turbulent jets. The main advantage of this model is its physical basis which provides a conceptual structure that draws together many different ideas and observations and also provides a tool which may help to explain new observations.

The authors wish to thank the Australian Research Council for the financial support of this project.

REFERENCES

ANTONIA, R. A. & BILGER, R. W. 1973 An experimental investigation of an axisymmetric jet in a co-flowing air stream. *J. Fluid Mech.* **61**, 805–822.

BEVILAQUA, P. M. & LYKOUDIS, P. S. 1978 Turbulence memory in self-preserving wakes. *J. Fluid Mech.* **89**, 589–606.

BILGER, R. W. 1968 The turbulent plane jet-wake. In *Proc. Third Australasian Conf. on Hydraulics and Fluid Mechanics, University of Sydney, Sydney Australia.*

BIRINGEN, S. 1986 An experimental investigation of a turbulent round jet in a coflowing airstream. In *Proc. ASME Winter Annual Meeting, Anaheim, California.*

BRADBURY, L. J. S. & RILEY, J. 1967 The spread of a turbulent plane jet issuing into a parallel moving airstream. *J. Fluid Mech.* **27**, 381–394.

BRANCHER, P., CHOMAZ, J. M. & HUERRE, P. 1994 Direct simulations of round jets: Vortex induction and side jets. *Phys. Fluids* **6**, 1768–1775.

CARMODY, T. 1964 Establishment of the wake behind a disc. *Trans. ASME* D: *J. Basic Engng* **86**, 869.

CHALLEN, J. 1968 Mixing in turbulent jet flows. Master's thesis University of Sydney.

CHEVRAY, R. 1968 The turbulent wake of a body of revolution. *Trans. ASME* D: *J. Basic Engng* **90**, 275.

CORRSIN, S. & KISTLER, A. L. 1955 Free-stream boundaries of turbulent flows. *NACA Tech. Rep.* 1244.

DAHM, W. J. A. & DIMOTAKIS, P. E. 1986 Measurements of entrainment and mixing in turbulent jets. *AIAA J.* **25**, 1216–1223.

GIBSON, M. M. 1963 Spectra of turbulence in a round jet. *J. Fluid Mech.* **15**, 161–173.

HENBEST, S. & YACOUB, E. 1991 A study of the flow in axisymmetric co-flowing jets. In *Intl Conf. on Experimental Fluid Mechanics, Chengdu, China.*

KOLMOGOROV, A. N. 1941 The local structure of turbulence in incompressible viscous fluid for very large Reynolds numbers. *C. R. Acad. Sci. URSS* **30**, 301.

LIEPMANN, D. & GHARIB, M. 1992 The role of streamwise vorticity in the near-field entrainment of round jets. *J. Fluid Mech.* **245**, 643–668.

MACZYNSKI, J. F. J. 1962 A round jet in an ambient co-axial stream. *J. Fluid Mech.* **13**, 597–68.

MARTIN, J. E. & MEIBURG, E. 1991 Numerical investigation of three-dimensionally evolving jets subject to axisymmetric and azimuthal perturbations. *J. Fluid Mech.* **230**, 271–318.

MARUŠIĆ, I., NICKELS, T. B. & PERRY, A. E. 1994 A comparative study of the spectra of turbulent jets and boundary layers at high wavenumber. In *Proc. 2nd ICEFM, Torino, Italy.*

PERRY, A. E. & CHONG, M. S. 1982 On the mechanism of wall turbulence. *J. Fluid Mech.* **119**, 173–217.

PERRY, A. E., HENBEST, S. M. & CHONG, M. S. 1986 A theoretical and experimental study of wall turbulence. *J. Fluid Mech.* **165**, 163–199.

SHLIEN, D. J. 1987 Observations of dispersion of entrained fluid in the self-preserving region of a turbulent jet. *J. Fluid Mech.* **183**, 163–173.

SMITH, D. J. & HUGHES, T. 1977 Some measurements in a turbulent circular jet in the presence of a co-flowing free stream. *Aero. Q.* **XXVIII**, 185–196.

TANI, I. & KOBASHI, Y. 1951 Experimental studies on compound jets. In *2nd Jap. Natl Congress for Appl. Mech.*

TOWNSEND, A. A. 1976 *The Structure of Turbulent Shear Flow.* Cambridge University Press.

UBEROI, M. S. & FREYMUTH, P. 1970 Turbulent energy balance and spectra of the axisymmetric wake. *Phys. Fluids* **13**, 2205–2210.

WINCKELMANS, G. S. & LEONARD, A. 1993 Contributions to vortex particle methods for the computation of three-dimensional incompressible unsteady flows. *J. Comput. Phys.* **109**, 247–273.

WYGNANSKI, I. & FIEDLER, H. 1969 Some measurements in the self-preserving jet. *J. Fluid Mech.* **38**, 577–612.